Hysteresis loops and the demagnetization process at 4.2 K for melt-spun $Nd_{13}Fe_{77}B_{10}$

1998 J. Phys.: Condens. Matter 10 389

(http://iopscience.iop.org/0953-8984/10/2/018)

J. Phys.: Condens. Matter **10** (1998) 389–399. Printed in the UK PII: S0953-8984(98)85590-2

Hysteresis loops and the demagnetization process at 4.2 K for melt-spun $Nd_{13}Fe_{77}B_{10}$

Jin Han-min†§, Y B Kim†, W S Park‡, M J Park‡ and Wang Xue-feng§

† Korea Research Institute of Standards and Science, Taejon 305-606, Korea

‡ Korea University, Seoul, Korea

§ Department of Physics, Jilin University, Changchun, 130023, People's Republic of China

Received 30 June 1997, in final form 6 October 1997

Abstract. Hysteresis loops of melt-spun $Nd_{13}Fe_{77}B_{10}$ cooled down at the remanent state were measured at 4.2 K. The loop for fields of $H_{max} = 6.4$ MA m^{-1} is characterized by low- and high-field steps. The loop for fields of $H_{max} = 4.0$ MA m^{-1} is very thin with only a low-field step and is shifted profoundly along the H-axes. The loops and the spin distribution during the demagnetization process were analysed by micromagnetic finite-element calculations. Quantitatively, the calculations reproduce the experimental loops fairly well. The spin distribution is fairly nonuniform, and a domain-wall-like distribution appears not only at some grain boundaries but also within some grains at the high-field step. The demagnetization proceeds by nonuniform reversion as a whole, and neither the model of single-domain reversion nor the model of domain-wall pinning in the grain boundary model describes the process appropriately.

1. Introduction

It is well established that melt-spun Nd–Fe–B alloys are isotropic, and their permanent magnetic properties are related to the extremely fine-grained structure of the tetragonal $Nd_2Fe_{14}B$ phase [1]. The $Nd_2Fe_{14}B$ has an easy c-axis at room temperature and an easy cone at 4.2 K. The cone angle is 32 degrees, and the four easy axes are on the $\langle 110 \rangle$ planes [2]. The grains are in contact with each other (nearly stoichiometric alloys [3]) or are surrounded by a very thin Nd-rich phase (hyper-stoichiometric alloys [4]). The magnetic properties of the alloys at room temperature have been analysed by the exchange-coupled single-domain model [5] and micromagnetic calculations [6].

This paper reports on the hysteresis loops for a melt-spun $Nd_{13}Fe_{77}B_{10}$ permanent magnet measured at 4.2 K. The loops and spin distribution during the demagnetization process are analysed by micromagnetic finite-element calculations using the Gaussian–Seidel method [7].

2. Experiments

An amorphous alloy of nominal composition $Nd_{13}Fe_{77}B_{10}$ was prepared by a single-wheel technique under an argon atmosphere. The surface velocity of the Cu wheel was 35 m s^{-1} and the alloy was 1 mm wide and $\sim$30 μm thick. The alloy was annealed at 950 K (specimen 1) or 970 K (specimen 2) for 10 min in a vacuum of 1×10^{-4} Torr. The specimens were confirmed to be $Nd_2Fe_{14}B$ single phase by x-ray diffraction. The strips

0953-8984/98/020389+11$19.50

were arranged into a 5 mm long, 3 mm wide, 30 μm thick rectangular shape. They were cooled down to 4.2 K at the remanent state after magnetization along the ribbon length direction in a pulsed field of $\sim$7 MA m^{-1} at room temperature. The hysteresis loops were measured along the ribbon length direction for fields of $H_{max} = 6.4$ and 4.0 MA m^{-1} by a high-field vibrating sample magnetometer (Janis 4500/150A).

3. Model and method of calculation

The model magnet is composed of $n \times n \times n$ cubic $Nd_2Fe_{14}B$ grains of dimension L. Both the c- and [100]-axes of the grains are randomly oriented. Each grain is exchange coupled with the six adjacent grains and is divided into $m \times m \times m$ cubic single-domain elements of equal dimension, so that the magnet is divided into $(n \times m)^3$ single-domain elements. The periodic boundary conditions hold for the magnet. By neglecting the magnetic stray-field energy [5], the total Gibb's energy is formulated as

$$G = \sum_i \left[F_K(i) + F_H(i) + \frac{1}{2} F_X(i) \right] \left(\frac{L}{m} \right)^3 \tag{1}$$

where $F_K(i)$, $F_H(i)$ and $F_X(i)$ are the magnetocrystalline anisotropy energy, Zeeman energy and the exchange energy for the ith element, respectively, i.e.

$$F_K(i) = K_1 \sin^2\theta(i) + K_2 \sin^4\theta(i) + K_3 \sin^4\theta(i) \cos[4\phi(i)] \tag{2}$$

$$F_H(i) = -\boldsymbol{J}_s(i) \cdot H \tag{3}$$

$$F_X(i) = -\frac{w}{\mu_0} \frac{m}{L} \sum_{adjac.} \boldsymbol{J}_s(i) \cdot \boldsymbol{J}_s(\text{adjacent element}). \tag{4}$$

Here, $\theta(i)$ and $\phi(i)$ are the polar angles of the magnetization of the ith element in the $\langle 100 \rangle$ coordinate system, and w/μ_0 is the effective exchange constant per unit boundary area. The intergrain exchange interaction is approximated to be the same as that of the interelement exchange interaction within a grain. The values of J_s, K_1, K_2 and K_3 were taken from [8, 9] and are listed in table 1.

Table 1. The values of J_s, K_1, K_2 and K_3 of $Nd_2Fe_{14}B$ at 4.2 K.

J_s [8] (T)	K_1 ($\times 10^6$ J m^{-3})	K_2 ($\times 10^6$ J m^{-3})	K_3 [9] ($\times 10^6$ J m^{-3})
1.86	−16	27	0.45

The magnetization of the magnet, J, was obtained from the minimum energy condition of each element $G(i)$, i.e.

$$\delta G(i) = \delta[F_K(i) + F_H(i) + F_X(i)] \geqslant 0 \qquad (i = 1, \ldots, (n \times m)^3). \tag{5}$$

The value of w/L was estimated by fitting the calculated ${}_iH_c$ with the experimental value.

The algorithm is as follows. Initially the magnet is saturated, then H is changed from H_{max} to $-H_{max}$ and then back to H_{max} by a step ΔH. At a given H, the first transitional angles of the ith element's magnetization, $\theta(i)$ and $\phi(i)$, are obtained from minimization of $G(i)$ within $\Delta\theta(i)$ $\Delta\phi(i) = 0, \pm d$ (d, angular step) under fixed magnetization of the other elements. For the new state of the ith element, the new transitional state is obtained for an adjacent element by the same way. After a cycle of such computation across all the $(n \times m)^3$ elements, G, the sum of the absolute values of the changed steps of $\Delta\theta(i)$ and

$\Delta\phi(i)$, $S = \sum_i(|\Delta\theta(i)| + |\Delta\phi(i)|)$, and the normalized magnetization of the magnet, J/J_s, are computed. With increase of the number of cycles nn, G and S decrease and $\{\theta(i), \phi(i)\}$ $(i = 1, \ldots, (n \times m)^3)$, G, S and J/J_s approach their limits. With the value of d being finite, their variation with nn is not always monotonic and in some cases is slightly fluctuating. The smallest value of G decreases with increase of nn, and the cycle of the computation was repeated until the occurrence of G larger than the smallest value was counted k times or S was decreased to zero.

Figure 1 demonstrates G, S and J/J_s as a function of nn calculated at $H = -0.8$ MA m^{-1} on the demagnetization curve for $n = 3$, $m = 7$, $w/L = 0.28$ and $d = 2$ degrees. All of G, S and J/J_s decrease monotonically with increasing nn, and the equilibrium state is reached at $nn = 602$, where S becomes zero. Table 2 demonstrates the small fluctuation of the G and nn dependences of k, G, S and J/J_s calculated at $H = 3.14$ and 0.24 MA m^{-1} on the same demagnetization curve.

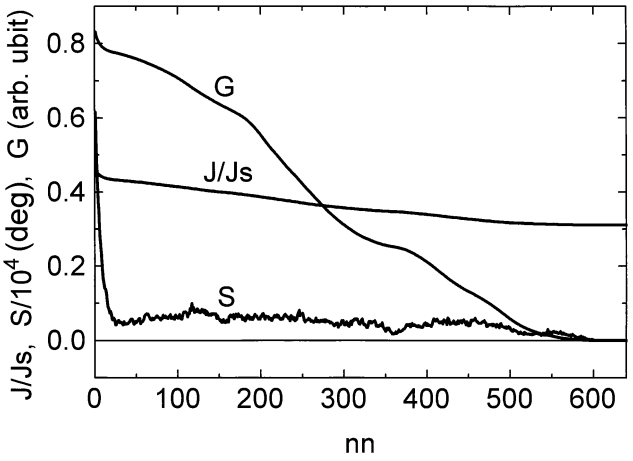

Figure 1. G, S and J/J_s as a function of nn at $H = -0.8$ MA m^{-1} on the demagnetization curve. $n = 3$, $m = 3$, $w/L = 0.366$ and $d = 2$ degrees.

The CPU time increases dramatically with increase of $n \times m$ and consumes more than one week for the computation of loop for $n \times m = 51$, $d = 2$ degrees and $k = 20$ (ALPHA SERVER 8200 5/300). The values of $n = 3$, $d = 2$ degrees, $\Delta H = 0.08$ MA m^{-1} (for the slowly-varying part of the loop) or 0.04 MA m^{-1} (for the steep part of the loop), and $k = 20$ were used throughout this work except when mentioned otherwise.

4. Results and analysis

4.1. Experimental results

Figure 2 shows the loop measured for fields of $H_{max} = 6.4$ MA m^{-1} for specimen 2. The two-step characteristics, which has been reported by previous authors [10, 11], is observed. The values of ${}_iH_c$ and $-H_i$, where the steepest part of the high-field step appears, are 2.1 and about -4.2 to -5.0 MA m^{-1}, respectively. For specimen 1, ${}_iH_c = 2.0$ MA m^{-1} is smaller while $H_i \approx 5.2$–6.0 MA m^{-1} is larger than those for specimen 2.

Table 2. G, J/J_s, S and k versus nn.

H (MA m^{-1})	nn	G (arbitrary unit)	J/J_s	S (deg)	k
3.14	1	−273 377.750	0.846	1120	
	10	−273 389.500	0.845	30	
	11	−273 389.500	0.845	16	1
	12	−273 389.531	0.845	12	
	13	−273 389.500	0.845	8	2
	14	−273 389.594	0.845	8	
	15	−273 389.531	0.845	6	3
	16	−273 389.594	0.845	6	4
	17	−273 389.531	0.845	6	5
	18	−273 389.594	0.845	6	6
	19	−273 389.531	0.845	6	7
	20	−273 289.594	0.845	6	8
	21	−273 389.531	0.845	6	9
	22	−273 389.594	0.845	6	10
0.24	1	−151 235.516	0.821	1900	
	12	−151 266.438	0.819	28	
	13	−151 266.438	0.819	8	1
	14	−151 266.484	0.819	6	
	15	−151 266.469	0.819	2	2
	16	−151 266.484	0.819	2	3
	17	−151 266.484	0.819	0	4

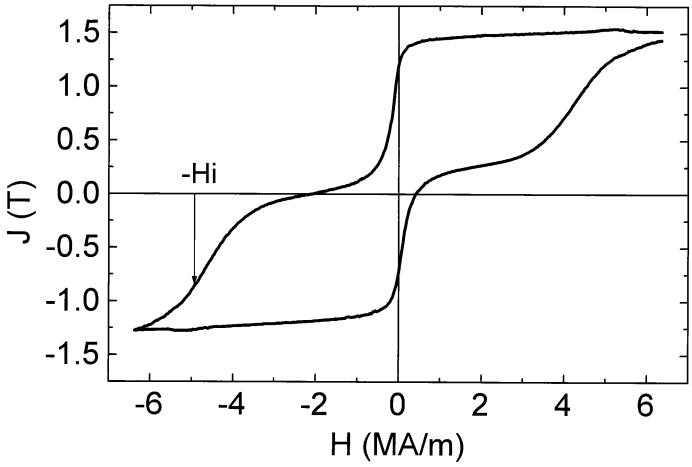

Figure 2. The hysteresis loop measured for fields of $H_{max} = 6.4$ MA m^{-1}.

Figure 3 shows the minor loop measured for fields of $H_{max} = 4.0$ MA m^{-1} for specimen 1. Only the low-field step is observed, and the loop is very thin. The loop is shifted profoundly along the H-axis intersecting the axis at -2.0 and -1.6 MA m^{-1}.

4.2. Analysis by single-domain models ($m = 1$)

Figures 4 and 5 show the major and minor ($H_{max} = 4.0$ MA m^{-1}) loops, respectively, computed by the Stoner–Wohlfarth (S–W) model ($w = 0$) for $n = 3$ and ∞, and by the exchange-coupled single-domain model ($w \neq 0$) for $n = 3$ and $w/L = 0.446$.

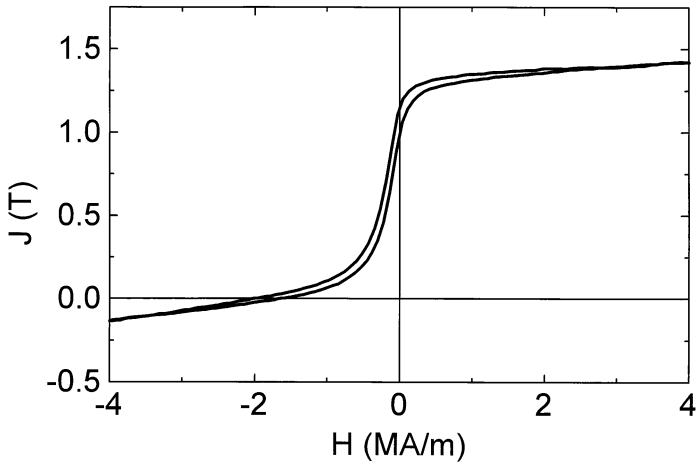

Figure 3. The minor hysteresis loop measured for fields of $H_{max} = 4.0$ MA m^{-1}.

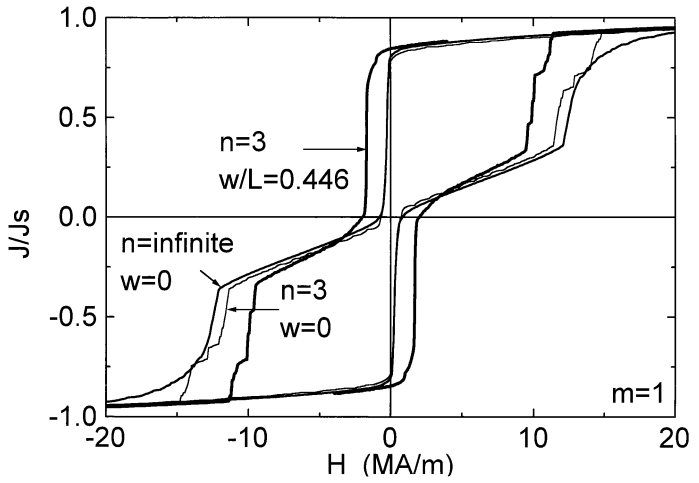

Figure 4. Major hysteresis loops computed for $n = 3$ and $w = 0$, $n = \infty$ and $w = 0$, and $n = 3$ and $w/L = 0.446$.

It is notable that the loops computed by the S–W model for such a small value of $n = 3$ are nearly the same as those for $n = \infty$. The S–W model reproduces the two-step characteristics of figure 2, and confirms that the low-field step is mainly due to the irreversible magnetization rotation around the cone and that the high-field step is due to the irreversible rotation from one cone to its oppositely-directed counterparts [11]. The value of ${}_iH_c = 0.6$ MA m^{-1} is much smaller than the experimental values of 2.0–2.1 MA m^{-1}, and $H_i \approx$ 12–15 MA m^{-1} is two or three times larger than the experimental values of 4.2–6.0 MA m^{-1}. The S–W model reproduces the upward shift of the minor loop along the J-axis, but fails in reproducing the shift along the H-axis.

The exchange-coupled single-domain model improves the simulation in respect to the leftward and rightward shift of the low-field and high-field step, respectively, and to the shift of the minor loop along the H-axis. The simulation of the loops on the whole, however, remains unsatisfactory.

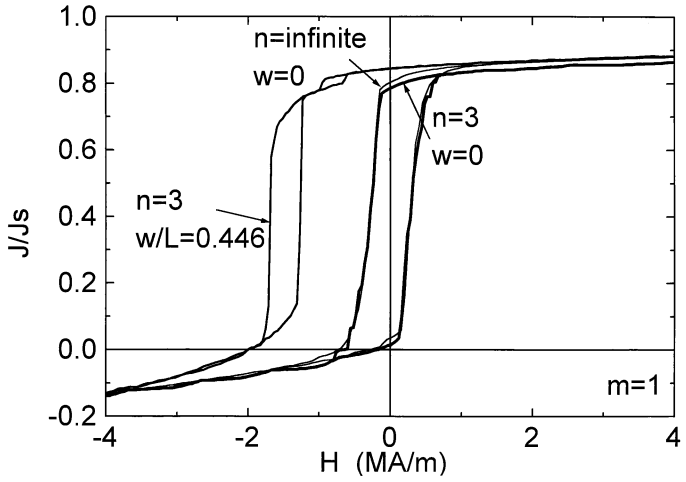

Figure 5. Minor hysteresis loops computed for $n = 3$ and $w = 0$, $n = \infty$ and $w = 0$, and $n = 3$ and $w/L = 0.446$.

4.3. Values of w/L

Figure 6 shows w/L as a function of m fitted for ${}_iH_c = \sim 2.0$ MA m^{-1} approximately. w/L decreases with increase of m and approaches the limit ~ 0.26. With $L \approx 30$ nm [1, 3], the exchange energy per unit area is estimated to be $wJ^2/\mu_0 \approx 0.02$ J m^{-2}. This value is consistent with $js^2/a^2 \approx 0.05$ J m^{-2} estimated from the experimentally observed domain wall width $\delta \approx 3$ nm [4] by using $\delta = \pi(js^2/2aK_1)^{1/2}$, $K_1 = 5 \times 10^6$ J m^{-3} [9] and $a \approx 0.2$ nm. Here, js^2 is the exchange energy for a pair and a is the distance between the pair.

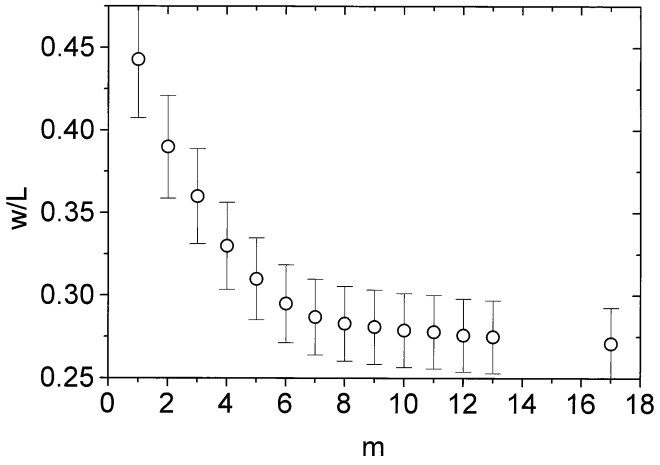

Figure 6. w/L versus m fitted for ${}_iH_c = \sim 2.0$ MA m^{-1}.

The values of $w/L(m)$ in figure 6 are used throughout this work unless otherwise mentioned.

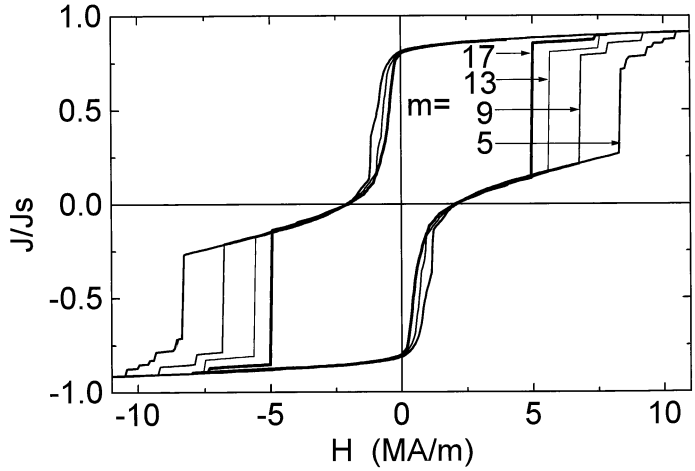

Figure 7. Major hysteresis loops computed for $m = 5$, 9, 13 and 17.

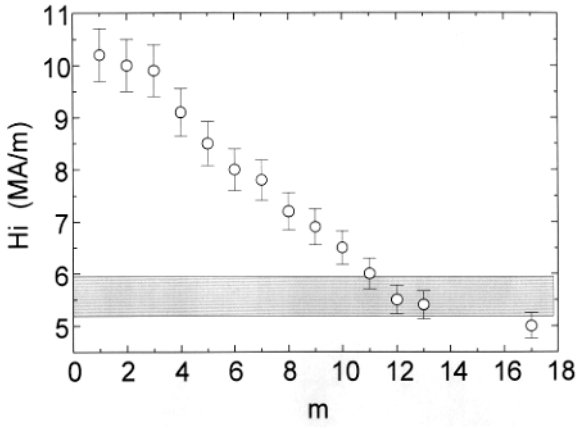

Figure 8. H_i as a function of m. The shaded area is the experimental result of $H_i = 5.2$–6.0 MA m^{-1} for specimen 1.

4.4. Simulation of the hysteresis loops by micromagnetism

Figure 7 shows the major loops computed for $m = 5$, 9, 13 and 17, and figure 8 presents the m dependence of H_i. With increase of m, H_i decreases and approaches the limit $\sim$5.0 MA m^{-1}, which is fairly close to the experimental value of 5.2–6.0 MA m^{-1} for specimen 1.

The two curves in figure 9 present the w/L dependence of ${}_iH_c$ and H_i, respectively, for $m = 17$. The shaded areas represent the experimental values of ${}_iH_c$ and H_i for specimens 1 and 2. With increase of w/L, ${}_iH_c$ increases but H_i decreases. ${}_iH_c = 2.0$ MA m^{-1} and $H_i = \sim$5.3 MA m^{-1} for $w/L = 0.25$, which are values in agreement with the experimental values of ${}_iH_c = 2.0$ MA m^{-1} and $H_i = 5.2$–6.0 MA m^{-1} for specimen 1. The larger value of $w/L = 0.29$ results in ${}_iH_c = 2.1$ MA m^{-1} and $H_i = 4.6$ MA m^{-1}, which are also in agreement with the experimental values of ${}_iH_c = 2.1$ MA m^{-1} and $H_i = 4.2$–5.0 MA m^{-1} for specimen 2.

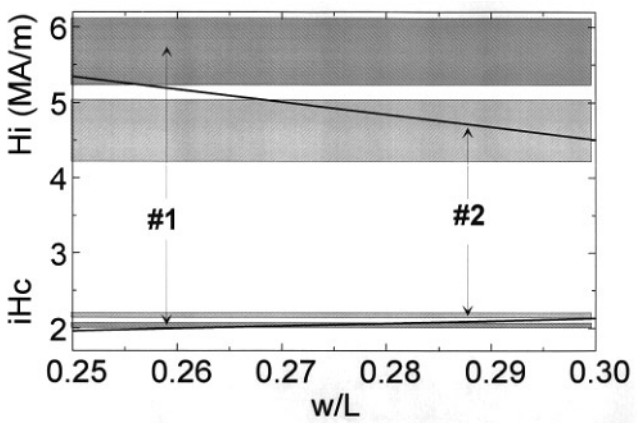

Figure 9. ${}_iH_c$ and H_i as a function of w/L for $m = 17$. The shaded areas are the experimental results for specimens 1 and 2.

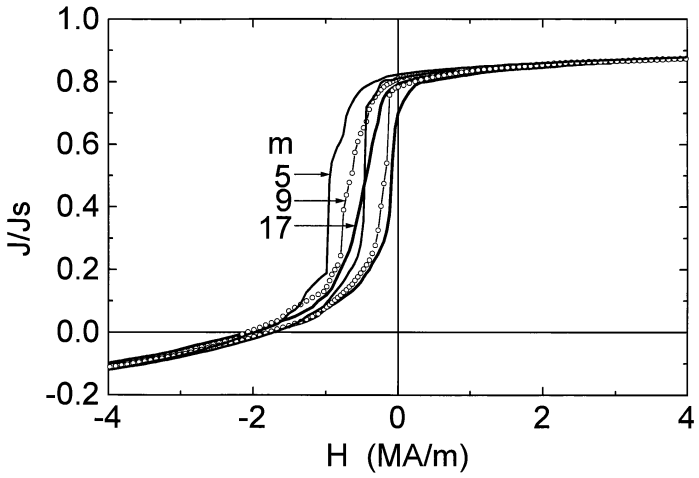

Figure 10. Minor hysteresis loops computed for $m = 5$ and $k = 80$, $m = 9$ and $k = 40$, and $m = 17$ and $k = 40$.

The high-field step is much steeper than in experiment, which is caused by neglect of the variety of grain size. The hysteresis loops for different grain sizes have different values of H_i (figure 9), and the superposition of the loops of different grain size results in a less steep high-field step. The range of the grain size distribution is estimated roughly as follows. The minimum and maximum values of H_i, $\sim$4.2 and $\sim$5.0 MA m^{-1}, for specimen 2 correspond to $w/L = 0.32$ and 0.27, respectively, from which it is deduced that $\Delta L/L(\text{average}) = 2(L_{max} - L_{min})/(L_{min} + L_{max}) \approx 20\%$.

Figure 10 shows the minor loops computed for $m = 5$, 9 and 17. With increase of m, the upper part of the low-field step shifts towards the H-axis improving the simulation. Although the loop is fairly thin, it is apparently broader than in experiment. The discrepancy may be caused by the following reasons: (i) the value of K_3 was estimated very roughly for fields as low as $H_{max} = 1.6$ MA m^{-1} [9]; (ii) the expression of the anisotropy energy in equation (2) is too inaccurate for $Nd_2Fe_{14}B$ at 4.2 K. The crystalline electric field analysis

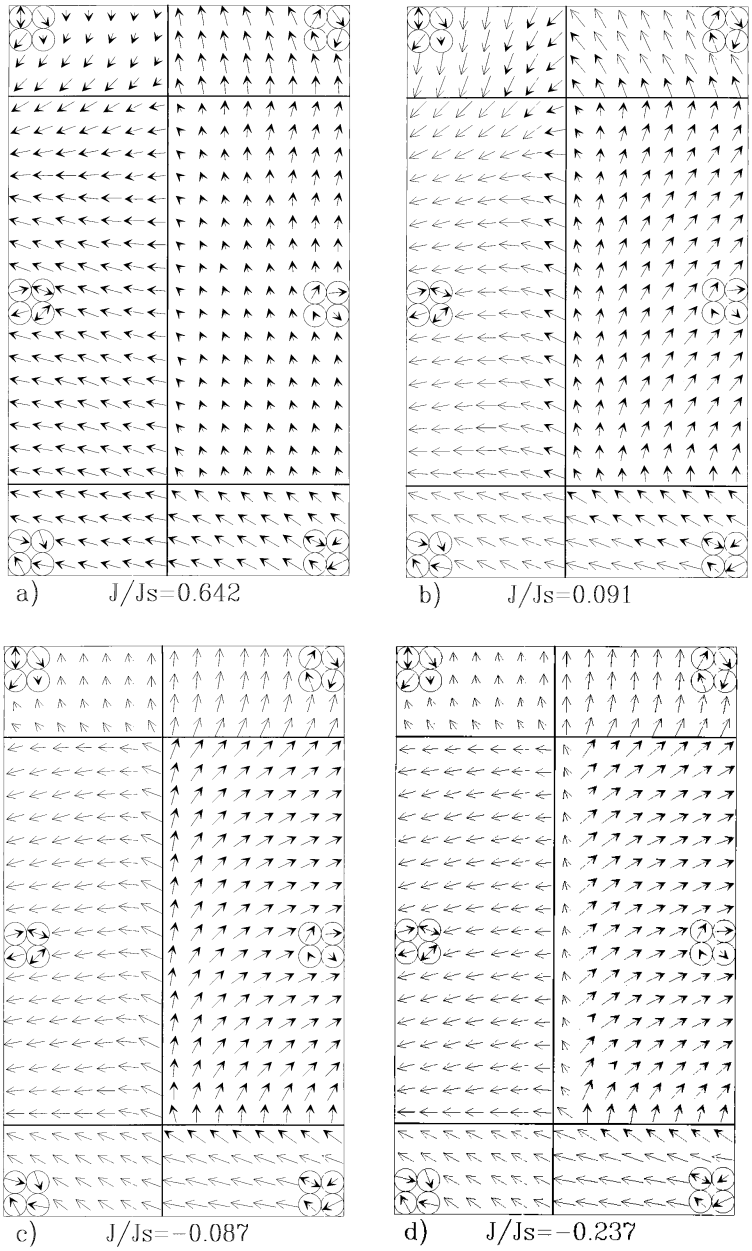

Figure 11. The $\boldsymbol{J}(\boldsymbol{r})/J_s$ distribution at the states of (a) $J/J_s = 0.642$ (upper part of the low-field step), (b) $J/J_s = 0.091$ (lower part of the low-field step), (c) $J/J_s = -0.087$ (between the low- and high-field steps), (d) $J/J_s = -0.237$ (upper part of the high-field step), (e) $J/J_s = -0.538$ (middle of the high-field step) and (f) $J/J_s = -0.885$ (at $H = -6.4$ MA m^{-1} after the high-field step is over).

on the single crystal of $Nd_2Fe_{14}B$ shows that the term $K_5 \sin^6\theta \cos 4\phi$, among other things, is important in characterizing the in-plane anisotropy [12], and therefore the width of the minor loop.

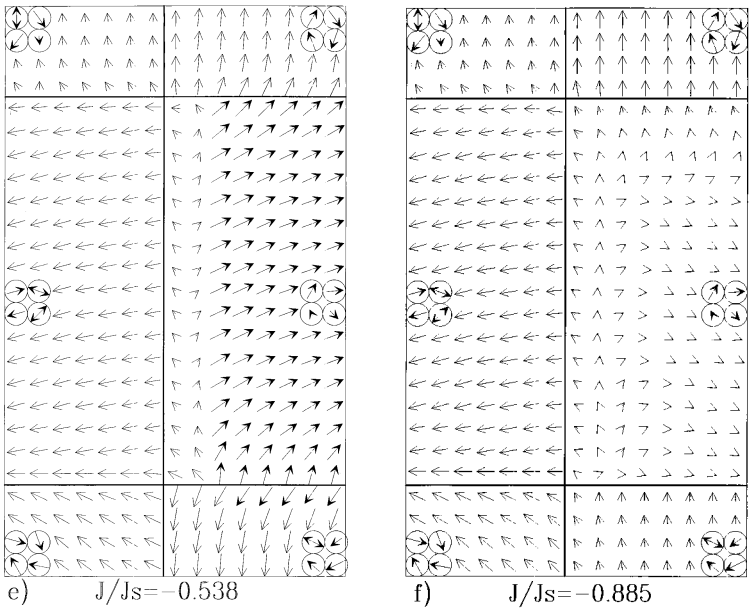

Figure 11. (Continued)

4.5. Spin distribution and the demagnetization process

Figures 11(a)–(f) show the unit magnetic vector distribution $\boldsymbol{J}(\boldsymbol{r})/J_s$ ($\boldsymbol{r}$, position vector) for part of six grains at different states during the demagnetization process computed for $m = 17$. These states are (a) $J/J_s = 0.642$ (upper part of the low-field step), (b) $J/J_s = 0.091$ (lower part of the low-field step), (c) $J/J_s = -0.087$ (between the low- and high-field steps), (d) $J/J_s = -0.237$ (upper part of the high-field step), (e) $J/J_s = -0.538$ (middle of the high-field step) and (f) $J/J_s = -0.885$ (at $H = -6.4$ MA m^{-1} after the high-field step is over). The section was cut at the middle of the magnet parallel to the magnet surface which is perpendicular to the applied field. The bold lines represent the grain boundaries. The arrows inside the four circles in each grain are the unit easy direction vectors, and the others represent $\boldsymbol{J}(\boldsymbol{r})/J_s$. The length of an arrow represents the projection on the section. The bold and thin arrows show that the projection of the vector in the positive field direction is positive and negative, respectively. The diameter of a circle represents the magnitude of a unit vector.

The main characteristics of the $\boldsymbol{J}(\boldsymbol{r})$ distribution and the demagnetization process are as follows.

(1) The domain-wall-like distribution of $\boldsymbol{J}(\boldsymbol{r})$ at grain boundaries persists in the second quadrant (figure 11(a)).

(2) Since there are eight easy directions and the direction of $\boldsymbol{J}(\boldsymbol{r})$ may be quite different near different grain boundaries, the $\boldsymbol{J}(\boldsymbol{r})$ distribution may be fairly nonuniform in a grain (middle-right grain in figures 11(c)–(e)).

(3) The domain-wall-like distribution of $\boldsymbol{J}(\boldsymbol{r})$ occurs not only at some grain boundaries but also within some grains in the third quadrant (figures 11(d) and (e)).

(4) The assertion by the S–W model in subsection 4.2 concerning the demagnetization process at the low- and high-field steps is true only in general. For some grains, the reversion

of $\boldsymbol{J}(\boldsymbol{r})$ to around the easy direction nearest to the negative field direction finishes before H decreases to $-H_i$ (upper-left grain in figure 11(c)).

In summary, the micromagnetic finite-element calculations simulate quantitatively the hysteresis loops fairly well. The demagnetization process is a nonuniform reversion as a whole. Neither the model of the coherent reversion of single domains nor the model of wall pinning at the grain boundaries describes the magnetization process properly for the nanocrystalline magnet, at least at low temperatures.

Acknowledgments

This work was supported by the Brain Pool Project of the Korean Federation of Science and Technology Societies and the National Science Foundation of China.

References

[1] Manaf A, Buckley R A, Davies H A and Leonowicz M 1991 *J. Magn. Magn. Mater.* **101** 360
[2] Cadogan J M, Gavigan J P, Givord D and Li H S 1988 *J. Phys. F: Met. Phys.* **18** 779
[3] Clemente G B, Keem J E and Bradley J P 1988 *J. Appl. Phys.* **64** 5299
[4] Mishra R K 1986 *J. Magn. Magn. Mater.* **54**–**57** 450
[5] Fukunaga H and Inoue H 1992 *Japan. J. Appl. Phys.* **31** 1347
[6] Fisher R, Schrefl T, Kronmuller H and Fidler J 1996 *J. Magn. Magn. Mater.* **153** 35
[7] Torre E D 1986 *IEEE Trans. Magn.* **22** 484
[8] Hirosawa S, Matsuura Y, Yamamoto H, Fujumura S, Sagawa M and Yamauchi M 1986 *J. Appl. Phys.* **59** 873
[9] Yamauchi H, Yamada M, Yamaguchi Y, Yamamoto H, Hirosawa S and Sagawa M 1986 *J. Magn. Magn. Mater.* **54**–**57** 575
[10] Hadjipanayis G C and Kim A 1987 *IEEE Trans. Magn.* **23** 2533
[11] Pinkerton F E 1988 *J. Appl. Phys.* **64** 5565
[12] Yu Yan, Jin Han-min and Zhao Tie-song 1966 *J. Magn. Magn. Mater.* **164** 201